RSC Advances

PAPER

View Article Online
View Journal | View Issue

Cite this: *RSC Adv.*, 2017, **7**, 21607

Sintering of multiple Cu–Ag core–shell nanoparticles and properties of nanoparticle-sintered structures†

Jiaqi Wang and Seungha Shin *

Received 3rd March 2017
Accepted 3rd April 2017

DOI: 10.1039/c7ra02611k

rsc.li/rsc-advances

Cu–Ag core–shell (CS) nanoparticles (NP) have been synthesized to replace pure Ag NP paste in order to lower the cost while maintaining excellent thermal and electrical conductivities for electronic applications. In this study, a multiple-CS-NP sintering model with molecular dynamics is employed to investigate the NP size and temperature dependency of the sintering process, as well as mechanical and thermodynamic properties of the sintered structures. Porosity and multiple particle effects are included, which allow for more accurate analysis than the conventional two- or three-NP sintering model. We unravelled the sintering mechanism at room temperature, and the interplay of liquid and solid surface diffusion during sintering at higher temperatures. Interfacial atoms have a higher mobility than surface atoms and contribute to a higher densification in the multiple-CS-NP model. A more densified structure yields higher Young's modulus, yield strength and Poisson's ratio, while lowering isothermal compressibility. The coefficient of thermal expansion and specific heat capacity exhibit grain-size and porosity independence. This multiple-CS-NP model provides a theoretical basis for determining NP configuration and sintering conditions for desirable properties.

Introduction

The miniaturization of electronic devices increasingly motivates the development of nanotechnology in synthesis, assembly, and the joining of metallic nanoparticles (NP).[1–7] Among them, Ag NP have been widely produced and employed in the fabrication of flexible and low-cost electronic devices through sintering, where high thermal and electrical conductivities are required.[8–12] However, the cost of Ag has increased significantly over the last few years and is not projected to display a reduction trend in the near future,[13] which has limited the wide industrial applications of Ag NP. Thus, Cu–Ag core–shell (CS) NP have been synthesized as a potential alternative to pure Ag NP;[14–16] this allows for the tremendous reduction of production costs, enhanced protection of the Cu core from oxidation, and thereby maintaining the desirable thermal and electrical properties for electronic applications.

Joining of the CS NP has been widely used as a bottom-up nanotechnology to provide permanent unions or connections to form functional nanodevices.[4] The main challenge to nano-joining lies in the formation of a robust junction between NPs with excellent mechanical, thermal, and electrical performances. Understanding the underlying sintering mechanisms of NPs can enhance the performance of the sintered structure through the manipulation of temperature, pressure, heating rate, NP size or relative crystallographic orientation. Numerous studies have been conducted on the sintering process of NPs both computationally and experimentally.[17–22] While most studies have focused on the monometallic two- or three-NP sintering model, the sintering process of multiple bimetallic Cu–Ag CS NPs is still relatively unexplored. The two- or three-NP sintering model is valid for loosely packed NP sintering in the gas phase or on substrates, but they overlook important factors that affect sintering dynamics and the properties of sintered structures.[23] For instance, agglomeration and pore effects, which significantly contribute to the sintering rate and porosity of final sintered structures, are neglected in the two-NP model.[24] Consequently, the sintering mechanisms and properties of sintered structures of multiple NPs are different from a two- or three-NP model. Therefore, a model containing pores to simulate the real case is essential for elucidating the sintering mechanism of the porous structure and studying the porosity dependency of sintered structure properties.

As an initial attempt, we developed a multiple-CS-NP sintering model with molecular dynamics (MD) simulation to gain

Department of Mechanical, Aerospace and Biomedical Engineering, The University of Tennessee, Knoxville, Tennessee, 37996-2210, USA. E-mail: sshin@utk.edu

† Electronic supplementary information (ESI) available: Final morphology of sintered multiple-CS-NP model $Ag_5Cu_{2.5}$ at different temperatures (Fig. S1); mean square displacement and cross-sectional images of multiple-CS-NP model with Ag_8Cu_4 and $Ag_{11}Cu_{5.5}$ (Fig. S2); final sintered structure of multiple Ag_5Cu_0 NPs at 600 K (Fig. S3); mean square displacement of the surface and shell atoms during the sintering of multiple $Ag_5Cu_{2.5}$ NPs (Fig. S4); stress–strain plots for four sintered structures (Fig. S5); potential energy evolution during the quenching process of the sintered structures (Fig. S6); isothermal compressibility of four sintered structures (Fig. S7); coefficient of thermal expansion of four sintered structures (Fig. S8). See DOI: 10.1039/c7ra02611k

insight into the nanoscale sintering process by monitoring the atomic movement.[17,25,26] Our model takes into account the effects of NP size and temperature in this research; we plan a further extension of this model to reveal the effects of pressure, size distribution and crystallographic orientation on the sintering process. The sintering simulations using the monometallic multiple-NP model have been confirmed to be very effective for reproducing the sintering process in porous anodes.[17,27] With this multiple-CS-NP model, the sintering dynamics of the CS porous structure at one atmospheric pressure but various temperatures, as well as mechanical and thermodynamic properties of sintered structures, are investigated effectively. Following this introduction, the methodology of simulation and analysis is displayed. In the Results and discussion section, the sintering dynamics and sintered structure properties are analysed and compared between (1) different-sized multiple-CS-NP models, (2) two-CS-NP and multiple-CS-NP sintering model, and (3) the bimetallic Cu–Ag CS NP model and monometallic pure Ag NP model. Implications and future work are elucidated in our conclusion.

Methodology

Modelling of multiple CS NPs

Differing from the two-CS-NP sintering model,[28,29] the multiple-CS-NP model possesses more degrees of freedom. Although particle packing arrangement can affect the sintering rate due to different numbers of contact points,[24,30] the sintering rate is not a main focus of this research and it is formidable and unnecessary to test all possible arrangements. Therefore, among various packing arrangements [*e.g.*, simple cubic (SC), body-centred cubic (BCC), face-centred cubic (FCC), hexagonal close-packed (HCP), *etc.*], we employed the SC arrangement, within which the NPs are facing each other with identical crystallographic orientation. For instance, we set the NPs facing each other with the [100] orientation in this research, then no other orientations such as [111] were induced in this SC arrangement. NPs were built within a simulation box with periodic boundary conditions in all three dimensions. Compared to the two-CS-NP sintering model under non-periodic boundary conditions,[29] this model is more realistic, since the agglomeration and porosity effect can be directly addressed.[17,24,27] To simplify the simulated system, the effects of core size, and size distribution of NPs were excluded; *i.e.*, all CS NPs in a simulation cell had the same radius and ratio of shell-thickness to core-radius.

The NP is denoted as Ag_xCu_y, where x and y represent the overall NP and core radii in terms of a_{Ag}, where a_{Ag} (= 4.079 Å) is the lattice constant of Ag. Four kinds of NP are employed; (1) NP1-Ag_5Cu_0, (2) NP2-$Ag_5Cu_{2.5}$, (3) NP3-Ag_8Cu_4, and (4) NP4-$Ag_{11}Cu_{5.5}$. The NP1-Ag_5Cu_0 is pure Ag NP with a radius of $5a_{Ag}$, and the latter three are Cu–Ag CS NPs with r_{cs} of $5a_{Ag}$, $8a_{Ag}$ and $11a_{Ag}$ and r_c of $2.5a_{Ag}$, $4a_{Ag}$, and $5.5a_{Ag}$. Therefore, the ratio of core radius to shell thickness remained as unity in CS NPs [*i.e.*, r_c: $(r_{cs} - r_c) = 1$].

Fig. 1a and b show the initial sintering configuration of multiple NP2-$Ag_5Cu_{2.5}$. Eight NPs are included in each simulation box: one (= 8 × 1/8) at eight corners, three (= 6 × 1/2) at the centres of the six faces, three (= 12 × 1/4) at the centres of the twelve edges, and one at the centre of the simulation box. The NPs are separated by a distance of a_{Ag} to prevent atoms from overlapping. This distance is still within the cut-off radius of the interaction potential so that the sintering can be initiated by attractive forces among the atoms. For analysis of the surface and shell diffusion during sintering, the NP is divided into three regimes: Cu core, Ag shell, and Ag surface (Fig. 1c); their atomic distances (r) from the centre of mass are in the range of $0 < r < r_c$, $r_c < r < r_{cs}$, and $(r_{cs} - a_{Ag}) < r < r_{cs}$, respectively.

Simulation methodology

In this research, all the simulations were performed utilizing the LAMMPS code,[31] and the Extreme Science and Engineering Discovery Environment (XSEDE) resources[32] were employed for partial simulations. The embedded atom method (EAM) potential[33] was applied for describing the interactions between Cu and Ag atoms.[34] This potential has been proven to accurately calculate the cohesive energy, lattice parameters, elastic constant, phase diagram and high-temperature properties of Cu and Ag. A timestep of 1 fs was chosen for all simulations, and Newton's equation of motion was integrated with the Verlet algorithm.[35]

Melting simulations were first performed to determine the melting temperature (T_m) as well as surface-premelting temperature (T_{sm}) of different-sized NPs. The simulation methodology was validated by comparing the obtained T_m with other reported values.[36] Based on the resulting T_{sm} and T_m, we selected temperatures for sintering simulations, in which we (1) investigated the temperature and size effect on the sintering dynamics, and (2) obtained final structures sintered at different temperatures as simulation subjects for the subsequent studies of mechanical and thermodynamic properties.

Melting simulations

For melting simulations, the system was equilibrated at 300 K for 50 ps, simulations were then continued at various temperatures ranging from 300 K to 1300 K (employing increments of 100 K from 300 K to 900 K, and increments of 20 K from 900 K to 1300 K for a closer observation near T_m) for 50 ps at each temperature, while recording the system-averaged potential

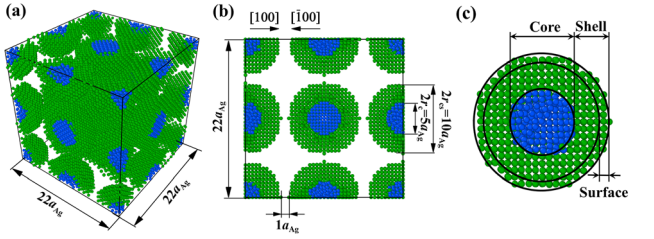

Fig. 1 (a) 3-D view of the initial configuration for sintering simulations of multiple NP2-$Ag_5Cu_{2.5}$. (b) Cross-sectional image of (a). The initial sintering arrangements of other CS NPs are identical to NP2-$Ag_5Cu_{2.5}$. (c) One CS NP2-$Ag_5Cu_{2.5}$ extracted from (a), which is divided into three regimes (core, shell, and surface), as illustrated. The Ag shell atoms are coloured with green, while the Cu core atoms are coloured with blue.

energy (E_p) and atom trajectories of the CS NP every 0.5 ps. Both the equilibration and data production phases were conducted in *NVT* canonical ensemble (constant number of atoms, volume, and temperature) with non-periodic boundary conditions. T_m was determined by the E_p curve; a sharp change in E_p indicated a phase transition.[37–40] Atom trajectories were processed to obtain the Lindemann index (δ_{LI}), which was employed to determine the T_{sm}. Also, the T_m was determined by δ_{LI} to verify the T_m determined by E_p. For a system consisting of N atoms, the system-averaged δ_{LI} is given by[41,42]

$$\delta_{LI} = \frac{2}{N(N-1)} \sum_{i<j} \frac{\sqrt{\left\langle R_{ij}^2 \right\rangle - \left\langle R_{ij} \right\rangle^2}}{\left\langle R_{ij} \right\rangle} \quad (1)$$

where R_{ij} is the distance between the i-th and j-th atoms and $\langle\ \rangle$ represents the ensemble average. Similar to E_p, a steep increase in the δ_{LI} curve was observed at T_m as the thermally-driven disorder increased significantly during the phase transition. Normally, δ_{LI}'s of 0.07 and 0.1 are utilized as melting criteria for Ag and Cu, respectively.[43] Thus, T_{sm} was determined, at which the δ_{LI} of surface atoms (Ag atoms) is above the melting criterion (0.07).

Sintering, diffusivity and activation energy

Sintering of four different multiple-CS-NP systems (NP1-Ag_5Cu_0, NP2-$Ag_5Cu_{2.5}$, NP3-Ag_8Cu_4, and NP4-$Ag_{11}Cu_{5.5}$) was simulated for 800 ps. All the initial sintering processes such as neck formation, growth, and densification were observed in the simulations. We employed the isothermal-heating method in sintering simulations;[44] *i.e.*, the sintering system was kept at 300 K for 800 ps using the 300 K relaxed structure, and then kept at 400 K for another 800 ps with the same structure, until the temperature reached 1300 K (with increments of 100 K). By applying the isothermal-heating method, temperature gradients inside the NP were eliminated, thus ignoring heat transfer effects. *NpT* isobaric–isothermal ensemble (constant number of atoms, constant pressure and temperature) was employed with Nosé–Hoover thermostat and barostat to control the system temperature and pressure (constant pressure of 1 atm at all temperatures). Sintering simulations were preceded by energy minimization on the initial multiple-CS-NP configuration with steepest decent algorithm.[45] Atom trajectory, E_p, densification (ξ, the ratio of reduction in volume of simulation cell to initial volume during sintering process), and mean square displacement ($\langle d^2 \rangle$) of surface and shell atoms were exported every 0.2 ps for further analysis. The $\langle d^2 \rangle$ was correlated with self-diffusivity (D_{self}) by Einstein's relation[46] given by

$$D_{self} = \frac{1}{2d} \lim_{\tau \to \infty} \frac{1}{\tau} \left\langle \left\{ [r(t_0+\tau) - r_{com}(t_0+\tau)] - [r(t_0) - r_{com}(t_0)] \right\}^2 \right\rangle \quad (2)$$

where d is the dimensionality, equivalent to 3 for our sintering system, τ is the elapsed observation time, $r(t)$ is the atomic position at time t, and $\langle \{[r(t_0 + \tau) - r_{com}(t_0 + \tau)] - [r(t_0) - r_{com}(t_0)]\}^2 \rangle$ is $\langle d^2 \rangle$, which has eliminated any effect from the random centre-of-mass motion caused by Nosé–Hoover thermostat and barostat. The angle brackets, $\langle\ \rangle$ indicate an ensemble average over all time origins t_0. Based on the above equations, the $\langle d^2 \rangle$ and D_{self} can be obtained by post-processing the atomic trajectory files. Additionally, the activation energy of surface and shell diffusion are obtained by fitting the temperature dependence of the D_{self} to the Arrhenius expression given by[25,47]

$$D_{self} = D_0 \exp\left(\frac{-Q_v}{RT}\right) \quad (3)$$

where Q_v is the activation energy, D_0 is a pre-exponential factor, and R is the universal gas constant (= 8.314 J K^{-1} mol^{-1}).

Mechanical properties

Before running simulations for mechanical properties, the final sintered structures (sintering products at 800 ps) were annealed from the sintering temperature (T_{sinter}) to room temperature (T_{room} = 300 K) within 100 ps, and the annealed structures were further relaxed at T_{room} for another 100 ps to obtain a fully equilibrated structure. Strain was then applied by uniformly extending the x dimension of the MD cell with a constant axial strain rate of 2×10^{-2} ps^{-1}; *i.e.*, extending the box length in the x dimension by 2% of its original length every picosecond, followed by rescaling the new x coordinates of the atoms to fit within the new dimension.

Strain (ε), stress (σ), and x, y, and z dimensions of the simulation cell were recorded every 0.2 ps during the tensile test for mechanical properties, including Young's modulus ($E_{100} = d\sigma/d\varepsilon$ in the elastic regime), yield strength (σ_{YS}), and Poisson's ratio ($\nu_{100} = -\varepsilon_{yy}/\varepsilon_{xx} = -\varepsilon_{zz}/\varepsilon_{xx}$). Since each NP was initially placed facing other NPs with the [100] direction and did not rotate during sintering, the E_{100}, σ_{YS} and ν_{100} obtained below T_m were regarded as those of the {100} faces in the final structures. The E_{100} and σ_{YS} were extracted from the strain–stress plots, while ν_{100} was obtained by calculating the strain ratio in the y (or z) direction and x direction (strain direction).

Thermodynamic properties

We performed MD simulations on calculating the isothermal compressibility (β_T), volumetric coefficient of thermal expansion (α_p), and constant-volume specific heat capacity (c_v), using the equations shown below:[48–50]

$$\beta_T = \left[-\frac{1}{V} \left(\frac{\partial V}{\partial p} \right) \right]_T \quad (4)$$

$$\alpha_p = \left[\frac{1}{V} \left(\frac{\partial V}{\partial T} \right) \right]_P \quad (5)$$

$$c_v = \left[\left(\frac{\left\langle E_{p,tot}^2 \right\rangle - \left\langle E_{p,tot} \right\rangle^2}{k_B T^2 m} \right) \right]_V \quad (6)$$

In eqn (4) and (5), V is the volume of the system, k_B is the Boltzmann constant (= 8.614×10^{-5} eV K^{-1}) in eqn (6), m is the mass of the NP-sintered structure, and $E_{p,tot}$ is the total potential energy of the system. The multiple-NP-sintered structures at different temperatures were equilibrated prior to the

simulations for β_T, similar to that in obtaining mechanical properties. Then, the multiple-NP-sintered structures were further simulated for 100 ps at T_{room} under five different pressures (81, 121, 161, 201, and 241 atm, respectively) within the *NpT* ensemble. As pressure increases, the NP-sintered structure is more compressed, thus decreasing the volume. The compressed volume was obtained by averaging the volume during the last 50 ps. The ratio of volume change to original volume ($-\Delta V/V_0$, where V_0 is the original volume at 1 atm) was plotted with respect to pressure change (Δp), and β_T was calculated using the slope of the plot obtained by eqn (4). In simulations for α_p calculation, the NP-sintered structure was first relaxed at a temperature 200 K lower than the T_{sinter} for 200 ps, then the temperature was increased by a step of 20 K and the system maintained at each increased temperature for 100 ps. The volume was averaged during the last 50 ps as well. The α_p is the slope of the $(-\Delta V/V_0) - \Delta T$ plot as in eqn (5). Since the c_v is dependent on T below the Debye temperature (215 K for Ag and 315 K for Cu, respectively),[51] we evaluated the c_v of all sintered structures at 300 K using eqn (6) after the equilibration to exclude the temperature dependency.

Results and discussion

Thermal stability of different-sized NPs

Sintering dynamics are affected by diffusion behaviours of single NP, which depend on the NP shape, size, temperature, *etc.* For example, thermal diffusion of triangular nanoplates can be activated at T_{room}, allowing the nanoplates to self-sinter and form nanobelts with a growth-oriented capping agent,[52] while the diffusion of the Cu–Ag CS spherical NP is not initiated at T_{room}.[29] Thus, thermal stability of NPs is first studied under the heating process by determining the critical temperatures such as T_m and T_{sm} according to the two aforementioned criteria: E_p (Fig. 2a) and δ_{LI} (Fig. 2b). Steep jumps are observed in both curves at 960 K, 1180 K, and 1220 K for NP2-$Ag_5Cu_{2.5}$, NP3-Ag_8Cu_4 and NP4-$Ag_{11}Cu_{5.5}$, respectively. The obtained T_m's for different sizes of Cu–Ag CS NPs coincide well with the reported computational values.[36] For further verification and comparison, we display the cross-sectional images of NP3-Ag_8Cu_4 in Fig. 2a. As temperature increases, the NP have a less crystallized structure, and the structure at the determined T_m is completely amorphous, also indicating the phase transition from solid to liquid.

The Lindemann atom, which has δ_{LI} larger than 0.07, on the Ag surface indicates that the surface is premelted, and it appears at temperatures of 900 K in NP2-$Ag_5Cu_{2.5}$ (Fig. 2c), 1100 K in NP3-Ag_8Cu_4 (Fig. 2d), and 1160 K in NP4-$Ag_{11}Cu_{5.5}$ (Fig. 2e), which are determined as T_{sm}. Since the pure Ag NP, *i.e.*, NP1-Ag_5Cu_0, has the identical size to NP2-$Ag_5Cu_{2.5}$, the NP1-Ag_5Cu_0 should have the same T_m and T_{sm} as the NP2-$Ag_5Cu_{2.5}$, which are 960 K and 900 K, respectively. As NP size increases, the portion of surface atoms with a lower coordination number decreases, which induces the increase in T_{sm}, the decrease in the surface energy, and thus the surface atom mobility. In addition to size effects, the Cu/Ag interface enhances the mobility of interfacial Cu and Ag atoms, which can make a difference in the sintering dynamics as compared to pure Ag NP sintering. Detailed physical analysis is demonstrated in the

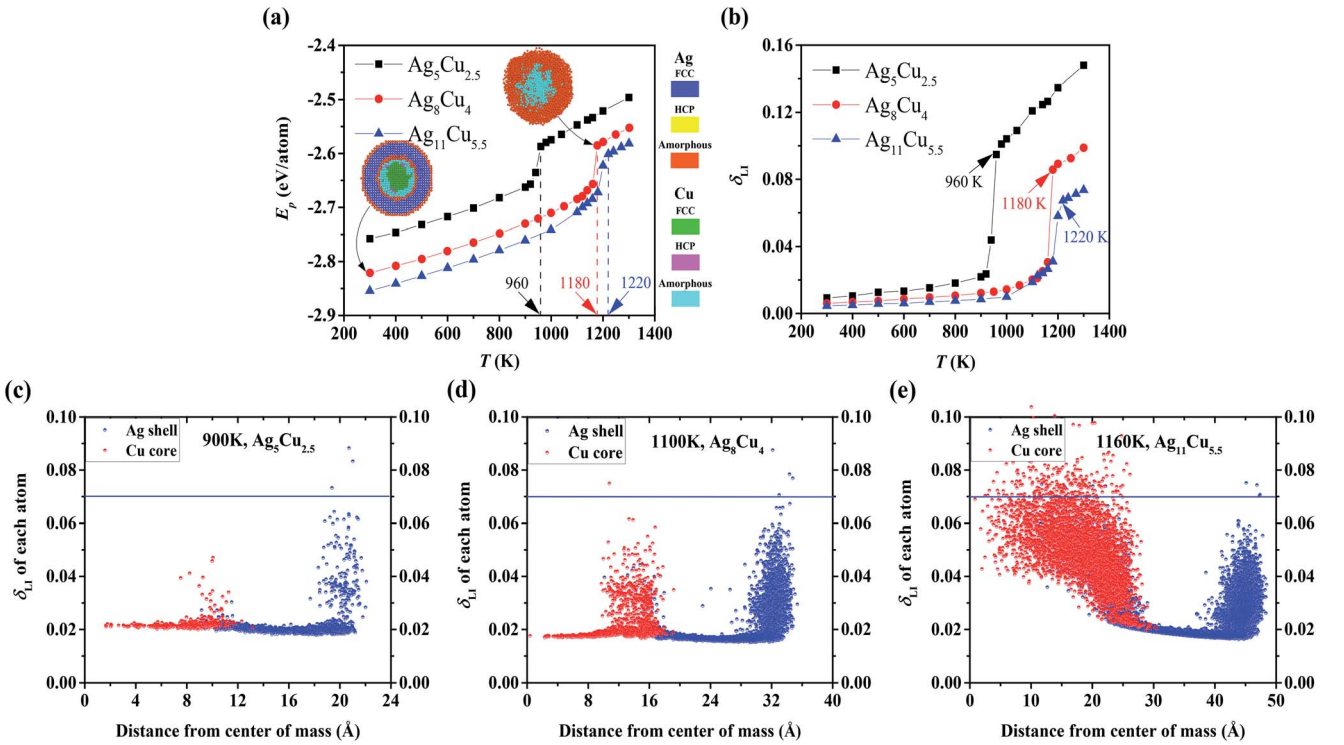

Fig. 2 (a) Potential energy (E_p) of different-sized single CS NP during the heating process. (b) Lindeman index (δ_{LI}) of different-sized single CS NP during the heating process. The melting temperatures (T_m) determined by both the E_p and δ_{LI} coincide well with each other. Radial distribution of δ_{LI} in (c) NP2-$Ag_5Cu_{2.5}$, (d) NP3-Ag_8Cu_4, and (e) NP4-$Ag_{11}Cu_{5.5}$ at surface premelting temperature (T_{sm}).

Table 1 Geometrical details, melting temperatures (T_m) and surface premelting temperatures (T_{sm}) for four NPs

NP type	r_{cs}	r_c	# Cu atoms	# Ag atoms	T_m (K)	T_{sm} (K)
NP1-Ag_5Cu_0	$5a_{Ag}$	0	0	2120	960	900
NP2-$Ag_5Cu_{2.5}$	$5a_{Ag}$	$2.5a_{Ag}$	369	1874	960	900
NP3-Ag_8Cu_4	$8a_{Ag}$	$4a_{Ag}$	1505	7505	1180	1100
NP4-$Ag_{11}Cu_{5.5}$	$11a_{Ag}$	$5.5a_{Ag}$	4093	19 401	1220	1160

section on the comparison between the sintering of Cu–Ag CS and Pure Ag NP. Table 1 summarizes the geometrical details and the corresponding T_m and T_{sm} for each NP.

Sintering dynamics of the multiple-CS-NP model

As the size of the NP decreases, the fraction of surface-layer atoms, which are more sensitive to the surrounding temperature,[42,53,54] increases. Thus, a smaller NP is more thermodynamically active as confirmed by their lower T_{sm} (Table 1). However, if the NP size is too small, the quantum-confinement effect should be considered,[55] which cannot be properly addressed in MD. Hence, for a clear observation of the temperature-effect on sintering dynamics while avoiding the quantum-confinement effect, the multiple-CS-NP model of $Ag_5Cu_{2.5}$ (the smallest NP in this research) is selected.

E_p is analysed not only for detecting the sintering mechanism, but also for evaluating the stability of the final sintered structures. As shown in Fig. 3a, the E_p of Ag shell atoms (obtained by averaging the E_p during last 50 ps) in the final structures sintered at different temperatures increases linearly as temperature increases from 300 K to 500 K, characterized as the low-temperature sintering without pore elimination (Fig. S1a–c†). The surface diffusion mechanism loses its dominance at low temperatures (300–500 K); instead, other mechanisms, such as plastic deformation involving dislocation or twinning, contribute to the densification.[24] Therefore, we employ 300 K as a low-temperature case for the multiple-CS-NP model. There is an obvious decrease in E_p of the Ag shell in structures sintered at a temperature between 600 K (pore elimination temperature, T_{pe}) and 800 K. This decrease is induced by the annihilation of free surface, due to pore elimination after sintering (Fig. S1d–f†). The E_p decrease indicates that a more stable structure is achieved in this temperature range ($T_{pe} < T < T_{sm}$), compared to the low-temperature cases. At 900 K (T_{sm}), the pores are eliminated with a higher speed since surface-premelting occurs in multiple NP2-$Ag_5Cu_{2.5}$ (Fig. S1g†). The whole NP system is melted at 1000 K (the T_m is 960 K for NP2-$Ag_5Cu_{2.5}$) and the final sintered structure is shown as Fig. S1h.† The melting is also indicated by a steep jump in E_p from 900 K to 1000 K (Fig. 3a). However, unlike the Ag shell, the E_p of the Cu core shows a linear increase both before and after melting, indicating that the Cu cores do not participate in the sintering at temperatures below T_m. Based on the above analysis, we only selected 300, 600, 900, and 1000 K to efficiently analyse the temperature effect on the sintering dynamics of the multiple-CS-NP model with NP2-$Ag_5Cu_{2.5}$ in detail.

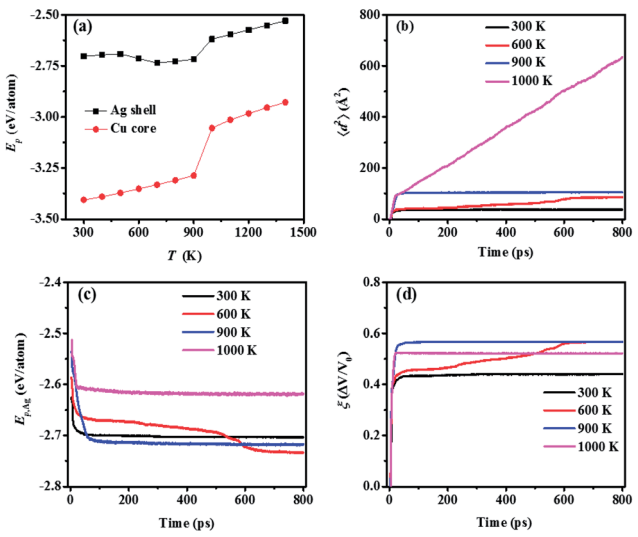

Fig. 3 (a) Averaged potential energy (E_p) of the Ag shell and Cu core over the last 50 ps (total simulation time: 800 ps) with respect to temperature. (b) Mean square displacement ($\langle d^2 \rangle$) of the surface atoms (atoms located within the depth of a_{Ag}) in multiple NP2-$Ag_5Cu_{2.5}$. (c) Potential energy of the Ag shell in NP $Ag_5Cu_{2.5}$ ($E_{p,Ag}$) at four representative temperatures (*i.e.*, 300, 600, 900 and 1000 K). (d) Densification (ξ) of the sintered structure of multiple NP2-$Ag_5Cu_{2.5}$. The trends of the $\langle d^2 \rangle$, $E_{p,Ag}$, and ξ coincide well with each other.

At each selected temperature, mean square displacement ($\langle d^2 \rangle$) of surface atoms, potential energy of Ag shell ($E_{p,Ag}$), as well as densification (ξ) of the sintering system were monitored during sintering, and plotted to characterize the sintering dynamics as in Fig. 3b–d. Regardless of temperature, the agglomeration of NPs involving neck formation and fast broadening was achieved within 20 ps as evidenced by the steep slopes of the curves in Fig. 3b–d. This indicates that the initial migration of atoms is not dominated by the thermal energy of the system. Instead, the attractive forces existing between the atoms lead to initial contact only if the distance between the NPs is less than the cut-off radius of the interaction potential. The finding of the temperature-independent initial stage in multiple-CS-NP sintering coincides well with our previous two-CS-NP sintering model, as well as many other MD simulations of sintering.[25,44,56–58]

The sintering process after the initial agglomeration shows a distinct T-dependence. At 300 K, $\langle d^2 \rangle$ of the surface atoms remains constant due to insufficient kinetic energy (E_k) for diffusion, leading to the equilibrium of E_p and ξ, while at 600 K, E_p and ξ do not reach the equilibrium. Continuous densification of the multiple NPs occurs at 600 K with a moderate speed, which facilitates the observation of various sintering mechanisms. A detailed illustration of the sintering process at 600 K is shown in

Fig. 4, during which the local order of each atom is identified by common neighbour analysis[59–61] and categorized as (1) FCC, (2) HCP and (3) amorphous (all other local orders, including BCC).

We monitored the sintering behaviour at 600 K from 5 ps, at which the NPs make their initial contact (Fig. 4a). The surface and partial inner Ag atoms of the centre NP (NP C, as indicated in Fig. 4) deviate from original FCC lattice sites to form several high-energy surface layers. As NPs approach one another, surface energy is minimized, necks are created and rapidly broadened within 5 ps, and the curvatures of the pores are diminished (Fig. 4b). Due to the pore-induced curvature and packing arrangement, elastic collision behaviour (collision and then bouncing back), which is observed in the two-CS-NP sintering model, is not detected in this multiple-CS-NP model. Although the neck formation and broadening stages reduce the curvature, the strong propensity for further reducing the curvature and thus the surface energy leads to further diffusion. In addition, because of the symmetry of the multiple-CS-NP system, the NPs located on the left and right of NP-C (NP-L and NP-R, respectively) can collide elastically with NP-C from both sides at the same time, which cancels the elastic collision behaviour. From 10 ps to 100 ps, amorphized atoms in the neck region rearrange themselves, leading to recrystallization and thus contributing to further E_p reduction. This detected amorphization–recrystallization coincides with both the CS two-NP and pure two-NP sintering model, such as nickel[62] and copper.[25] After 100 ps, pores are gradually diminished with a moderate E_p reduction rate until 600 ps, at which several stacking faults (double HCP layers) are formed. This multiple-CS-NP sintered structure reaches quasi-equilibrium after 700 ps, and stable stacking faults are left within the structure, which is potentially eliminated by the annealing process. The reduction of E_p at 600 K in Fig. 3c, acting as a driving force for the sintering,[19,63] contributes to densification comparable to that at 900 K, indicating that sintering at a lower T_{pe} can yield the same densification as high T. Note that the sintered structure at 600 K, even at 900 K, is not a fully densified structure, *i.e.*, some pores are still left in the structure.

Based on the $\langle d^2 \rangle$ value (Fig. 3b), solid surface diffusion is observed only at 600 K after the initial neck formation and growth stage. A dominant mechanism at T_{room} is not the solid surface diffusion, but the plastic deformation, including stacking deformation and twin boundary formation during the neck formation and growth. At T_{sm} (900 K), pores in the multiple-CS-NP system are quickly eliminated due to a higher mobility of premelted surface atoms. This irreversible pore elimination locates the system in a quasi-equilibrium low-energy state; thus, the premelted atoms recrystallize without diffusion, due to insufficient kinetic energy (E_k).

Surface and bulk diffusion of atoms dominate the liquid phase sintering at T_m (1000 K). The sintering process is dominated by the inter-diffusion of melted core and shell atoms, similar to that of the two-CS-NP sintering model at T_m.[29] The sintering product is an alloy structure with well mixed Cu and Ag atoms. The ξ of the final structure at 1000 K (Fig. 3d) is smaller (*i.e.*, larger volume) than that at 900 K, and even smaller than that at 600 K, due to the thermal expansion of the alloy.

In order to validate the reliability of our results and investigate the size effect, we performed sintering simulations with identical sintering conditions, but with different NP sizes, *i.e.*, the multiple-CS-NP sintering model with NP3-Ag_8Cu_4 and NP4-$Ag_{11}Cu_{5.5}$, $\langle d^2 \rangle$ and the corresponding final sintered structures of these two multiple-CS-NP sintering models at each temperature are shown in Fig. S2.† At T_{room}, it is commonly observed that the plastic deformation precedes others in the sintering process, especially at the initial stages. In the multiple-CS-NP system of NP3-Ag_8Cu_4, the solid surface diffusion dominates sintering at a temperature (900 K is tested for multiple-CS-NP Ag_8Cu_4) lower than its T_{sm} (Fig. S2a†). Since pores are eliminated at T_{sm} and a stable structure is formed (Fig. S2c†), the liquid

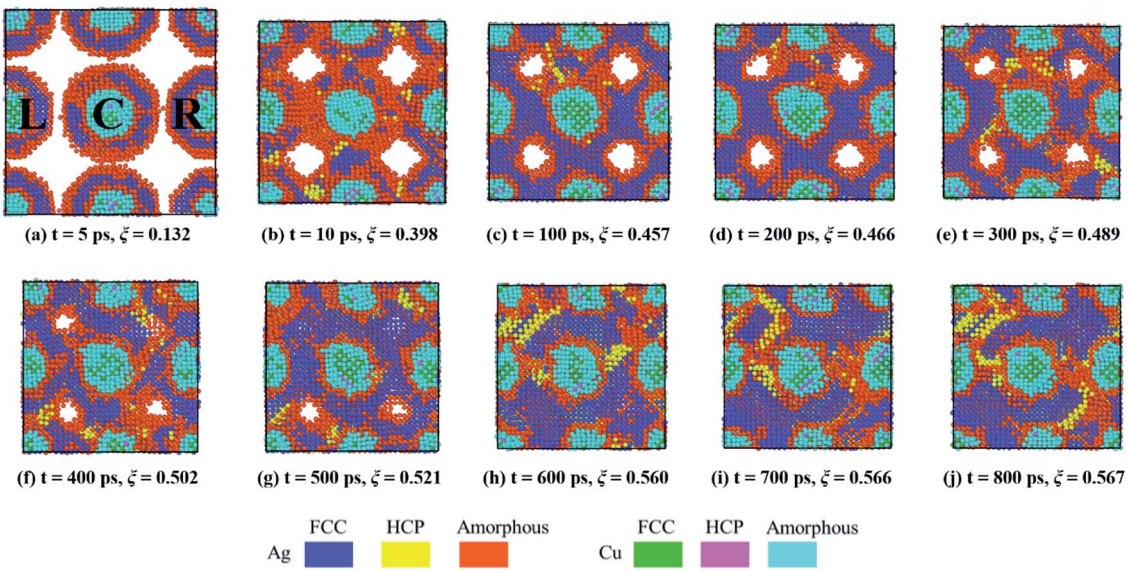

Fig. 4 Cross-sectional images of the sintering process of porous multiple NP2-$Ag_5Cu_{2.5}$ at 600 K. Blue: Ag FCC; yellow: Ag HCP; red: Ag amorphous; green: Cu FCC; magenta: Cu HCP; cyan: Cu amorphous.

surface diffusion at T_{sm} is deactivated. However, for the multiple-CS-NP model with $Ag_{11}Cu_{5.5}$, pores are not eliminated even at T_{sm} (1160 K, Fig. S2d†). As a result, solid surface diffusion dominates the sintering both at a lower temperature (1100 K is tested for multiple-CS-NP $Ag_{11}Cu_{5.5}$) and T_{sm} (Fig. S2b†).

Comparison between the sintering of Cu–Ag CS and pure Ag NPs

Sintering simulations on multiple NP1-Ag_5Cu_0 under the same conditions (size, temperature and pressure, *etc.*) as multiple NP2-$Ag_5Cu_{2.5}$ demonstrate that the CS NP is a more suitable candidate for higher ξ as shown in Fig. 5a–c. Since the CS and pure Ag NPs have the same overall radius, the higher ξ of CS NP is not induced by the higher mobility of surface atoms. $\langle d^2 \rangle$ of the surface atoms in both the CS and pure Ag NPs presents direct evidence for the similar mobility of surface atoms at T_{room} (black and green lines, Fig. 5d). However, the mobility of the overall shell atoms in the multiple-CS-NP model is over 60% higher than that of the pure Ag NP (blue and red lines, Fig. 5d–f), where this increased shell mobility is attributed to the lattice mismatch and interfacial restructuring between Ag and Cu atoms;[64] thus, the mobility of Ag atoms in the vicinity of the Cu–Ag interface is much higher than surface atoms. As the temperature increases to 600 K, pores are not eliminated (Fig. S3†) in pure Ag NP sintering, due to a lack of sufficient solid surface diffusion (smaller $\langle d^2 \rangle$ of pure Ag NP than the CS NP is demonstrated in Fig. 5e). Pore elimination at 600 K in the multiple-CS-NP model suggests that the activated interfacial Ag atoms facilitate the densification. At 900 K, even though surface premelting occurs in CS NP, the $\langle d^2 \rangle$ of the surface atoms is smaller than the pure Ag (black and green lines, Fig. 5f). This supports the conclusion that the surface diffusion is not a dominant mechanism at T_{sm} in small CS NP ($r_{cs} < 8a_{Ag}$), while it contributes to the densification of pure Ag NP at 900 K.

Self-diffusivity and activation energy

Self-diffusivity (D_{self}) characterizes atom mobility during sintering, and activation energy (Q_v) is a good measure of sinterability within porous materials.[23] D_{self} and Q_v for surface and shell diffusion in the multiple-CS-NP sintering model with $Ag_5Cu_{2.5}$ are calculated in this research. Accurate diffusivity can be obtained only if the atoms travel a sufficient distance to make the $\langle d^2 \rangle$ have a linear, infinite time behaviour, which is required by the Einstein's relation. However, below T_m, the atoms vibrate around the equilibrium positions once the sintering system reaches the minimum-energy state; *i.e.*, diffusion ends before it reaches linearity. Thus, $\langle d^2 \rangle$ is recorded during the diffusion period (between the initial contact of multiple NPs and the system minimum-energy state) for calculation of D_{self} and Q_v (starting and ending points of the diffusion period are indicated by spherical dots in Fig. S4a and b†). In Fig. 6, the Q_v of the shell and surface diffusion are 0.42 eV and 0.46 eV, respectively, which are in a fairly good agreement with the reported Q_v for the silver {100} surface diffusion (0.4 eV).[65]

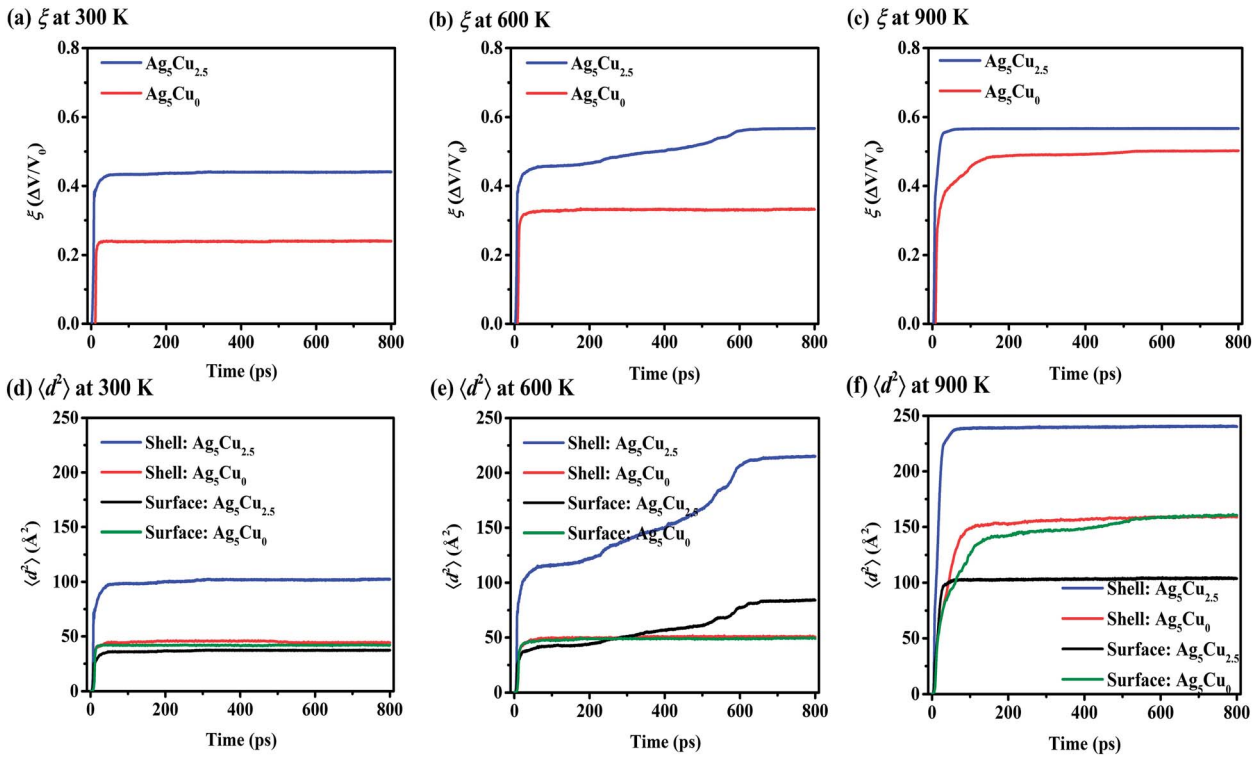

Fig. 5 (a–c) Densification (ξ) and (d–f) mean square displacement ($\langle d^2 \rangle$) during multiple-NP sintering with $Ag_5Cu_{2.5}$ and Ag_5Cu_0 at 300 K, 600 K, and 900 K. At each temperature, the ξ of CS NP2-$Ag_5Cu_{2.5}$ is higher than that of pure Ag NP1-Ag_5Cu_0 due to the high mobility of interfacial Ag atoms in the CS NP model.

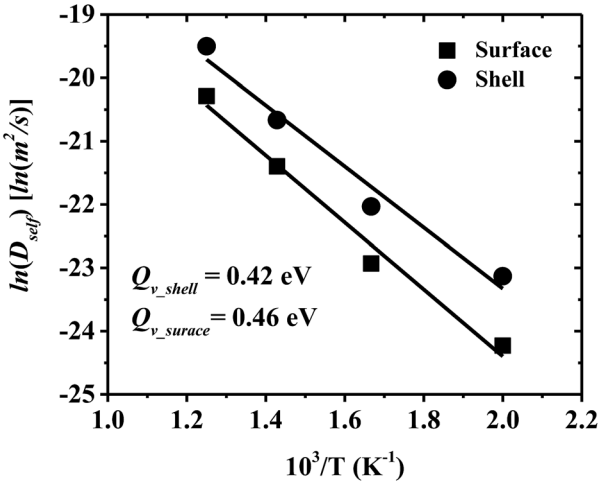

Fig. 6 Arrhenius plot of self-diffusivity of shell and surface in the multiple-CS-NP sintering model $Ag_5Cu_{2.5}$. The solid line is the Arrhenius equation fitting. The activation energies obtained for the shell and surface are 0.42 eV and 0.46 eV, respectively.

However, these values are smaller than the Q_v of the grain boundary (84.4 kJ mol^{-1} = 0.87 eV)[66] and lattice self-diffusion (192.1 kJ mol^{-1} = 1.99 eV)[67] in Ag. These discrepancies can be attributed to (1) a higher surface mobility induced by the ultrafine size, and (2) a higher mobility of interfacial Ag atoms in CS structures. Note that the Q_v of the overall shell is lower than that of the surface; *i.e.*, the shell diffusion is easier to be activated, compared to the surface only. These results also coincide with our previous findings that the interfacial atoms of the Ag shell have a higher mobility than surface atoms and lead to a much higher densification in Cu–Ag CS NP, as compared to same-sized pure Ag NPs. Smaller D_{self} and higher Q_v are expected for larger NPs due to the size effect, although significant size effect has not been reported on surface diffusivity for Ag NP in the size range of 10–40 nm.[68] More detailed examination of the size dependency of the activation energy will be conducted with the MD approach in the near future.

Mechanical properties

Sintering-temperature- and NP-size-dependent mechanical properties, including Young's modulus (E_{100}), yield strength (σ_{YS}), and Poisson's ratio (ν_{100}) are discussed in this section. Table 2 summarizes these properties of final structures sintered at four representative temperatures; (i) $T_1 = T_{room}$, (ii) $T_{room} < T_2 < T_{sm}$, (iii) $T_3 = T_{sm}$, and (iv) $T_4 > T_m$ (*i.e.*, 300, 600, 900, and 1000 K for both NP1-Ag_5Cu_0 and NP2-$Ag_5Cu_{2.5}$; 300, 900, 1100, and 1200 K for NP3-Ag_8Cu_4; 300, 1100, 1160 and 1300 K for NP4-$Ag_{11}Cu_{5.5}$). During the tensile test, isotropic shrinkage in the y and z directions is observed, demonstrating the identical Poisson's ratio in the final sintered structures. The strain–stress plots are shown in Fig. S5.†

Through scrutinized comparison and analysis, we have the following findings:

(1) Below T_m, all three properties (E_{100}, σ_{YS}, and ν_{100}) of the sintered structures by multiple NP1-Ag_5Cu_0 are smaller than the counterparts sintered by multiple NP2-$Ag_5Cu_{2.5}$. NP1 has a smaller elastic resistance, and its maximum force, which NP can bear for recovering the original shape, is also smaller; however, the resistance in the orthogonal directions of the strain are larger. Note that all of these properties also increase with sintering temperature, regardless of the NP size. This suggests that the pore narrowing and elimination in the final sintered product enhance its resistance to elastic deformation in the elongation direction, and the maximum force, while decreasing the resistance of deformation in the shrinkage directions.

(2) In general, all properties tend to decrease as the nanoscale grain size increases below T_{sm}. E_{100} of nanocrystalline materials increases with decreasing the grain size, which contradicts the previous study.[69] However, the porosity of the larger grain sized NP-sintered structure is also higher than the smaller grain-sized structure (even though the sintering temperature of the larger grain sized structure is higher), and the porosity has a substantially greater effect than grain size (larger porosity induces smaller E_{100}).[69] Therefore, a more dominant porosity effect leads to a smaller E_{100} in larger grain sized structures. The grain-size dependency of σ_{YS} and ν_{100} coincides well with previous experimental and theoretical results.[70,71]

(3) For the sintered structure above T_m, E_{100} and σ_{YS} are smaller than those at T_{sm}, except for the E_{100} of sintered NP4-$Ag_{11}Cu_{5.5}$. Pores in the sintered structure of multiple NP4-$Ag_{11}Cu_{5.5}$ are not eliminated at T_{sm}, leading to a smaller E_{100}, compared to that at the temperature (1300 K) above T_m. Quenching has been executed before the tensile test with rates

Table 2 Mechanical properties of the final structures sintered at four different temperatures

	Young's modulus (E_{100}, GPa)				Yield strength (σ_{YS}, GPa)				Poisson's ratio (ν_{100})			
T_{sinter} (K)	NP1	NP2	NP3	NP4	NP1	NP2	NP3	NP4	NP1	NP2	NP3	NP4
300	17.04	21.33	14.11	11.24	1.18	1.83	1.30	1.04	0.12	0.30	0.26	0.24
600	21.72	33.64	—	—	1.63	2.55	—	—	0.23	0.37	—	—
900	33.15	38.51	22.12	—	2.62	2.84	2.04	—	0.38	0.39	0.29	—
1000	27.72	33.22	—	—	1.63	1.51	—	—	0.40	0.41	—	—
1100	—	—	40.34	21.43	—	—	3.73	1.71	—	—	0.39	0.28
1160	—	—	—	23.37	—	—	—	2.13	—	—	—	0.31
1200	—	—	28.13	—	—	—	1.87	—	—	—	0.41	—
1300	—	—	—	34.05	—	—	—	1.68	—	—	—	0.41

Table 3 Thermodynamic properties (measured at 300 K) of four final structures (*i.e.*, NP1, NP2, NP3, and NP4) sintered at four different sintering temperatures (T_{sinter}'s)

	Isothermal compressibility (β_T, GPa^{-1})				Coefficient of thermal expansion [($\alpha_p \times 10^5$), K^{-1}]				Specific heat capacity (c_v, kJ kg^{-1} K^{-1})			
T_{sinter} (K)	NP1	NP2	NP3	NP4	NP1	NP2	NP3	NP4	NP1	NP2	NP3	NP4
300	0.099	0.053	0.068	0.095	5.50	6.43	6.69	6.48	0.051	0.134	0.122	0.122
600	0.068	0.014	—	—	6.07	6.50	—	—	0.055	0.122	—	—
900	0.017	0.010	0.041	—	7.40	7.26	5.90	—	0.056	0.111	0.150	—
1000	0.018	0.015	—	—	15.40	12.03	—	—	0.052	0.149	—	—
1100		—	0.009	0.049		—	7.14	6.848		—	0.128	0.167
1160		—	—	0.038		—	—	6.14		—	—	0.170
1200		—	0.008	—		—	12.02	—		—	0.132	—
1300		—	—	0.009		—	—	11.89		—	—	0.128

of 7×10^{12} K s^{-1}, 9×10^{12} K s^{-1}, and 10^{13} K s^{-1} for sintered multiple NP1-Ag_5Cu_0 and NP2-$Ag_5Cu_{2.5}$, NP3-Ag_8Cu_4, and NP4-$Ag_{11}Cu_{5.5}$, respectively, all of which are a few orders of magnitude higher than the critical quenching rate for glass formation (10^5 to 10^6 K s^{-1}).[72,73] The E_p evolutions during quenching (Fig. S6†) also indicate that all three sintered structures form metallic glass, without an abrupt decrease in the E_p curve.[74,75] The formation of the metallic glass yields lower E_{100} and σ_{YS}, compared to those of nanostructured porous materials. Contrarily, ν_{100} increases with temperature, regardless of whether the quenched structure is crystallized or metallic glass, which is different from the decrease of E_{100} and σ_{YS} at temperatures above T_m. A uniform ν_{100} of 0.41 is obtained for all metallic glass structures, manifesting the identical resistance in shrinkage direction.

Thermodynamic properties

Thermodynamic properties (*i.e.*, β_T, α_p, and c_v) calculated from our simulations are summarized in Table 3. The response of the volumetric change to pressure is more significant in a sintered structure with a larger porosity to yield a higher isothermal compressibility (β_T). At T_{room}, all four sintered structures possess large porosities, which induce large β_T (0.099, 0.053, 0.068, and 0.095 GPa^{-1} for NP1, NP2, NP3, and NP4 sintered structures, respectively), while β_T decreases with increasing T_{sinter} due to pore narrowing and elimination. Differing from sintered NP3 and NP4, β_T of the molten sintered structures of NP1 and NP2 are 0.018 $GPa^{-1}$and 0.015 GPa^{-1}, both of which are larger than those at T_{sm} of 900 K (0.017 $GPa^{-1}$and 0.010 GPa^{-1}, respectively). The sintered structures by multiple NP3's and NP4's still contain pores at T_{sm} (Fig. S2d†), but not at T_m. Thus, the β_T at T_{sm} is larger than for the molten sintered structures of NP3 and NP4. On the other hand, pores in NP1 and NP2 are completely eliminated above T_{sm}, so we attribute the larger β_T above T_{sm} to its lower crystallinity instead of porosity, which results in higher entropy and greater compressibility. This analysis concludes that porosity dominates the decreasing trend of β_T in the NP-sintered structure below T_{sm}, while the dominant factor switches to crystallinity once pores are completely eliminated.

α_p exhibits porosity and grain-size independence, *i.e.*, no obvious difference is observed for all NP-sintered structures below T_{sm}. A uniform α_p ($\sim 1.2 \times 10^{-4}$ K^{-1}) is achieved for all amorphous Cu–Ag alloy structure, which is ~75% higher than the α_p of the crystallized structure. Thus, the higher entropy of the less-crystallized melted structure induces not only more compressibility, but also more expansivity. Similar to α_p, no obvious dependency on porosity, grain size and crystallinity is detected for c_v. Values ranging from 0.111 to 0.170 kJ kg^{-1} K^{-1} are obtained for all CS NP-sintered structures, while a much smaller averaged c_v for the pure Ag NP sintered structure is calculated as 0.054 kJ kg^{-1} K^{-1}, induced by the larger atomic mass of Ag. The weak bonding existing between the Cu and Ag atoms may also contribute to higher c_v in CS sintered structures.

Conclusions

We report the sintering differences and similarities between (1) the different-sized multiple-CS-NP model, (2) the multiple Cu–Ag CS NPs and two Cu–Ag CS NPs models, and (3) the multiple Cu–Ag CS NPs and multiple Ag NPs models. The interplay among porosity, grain size, and crystallinity on the mechanical and thermodynamic properties of NP-sintered structures are also unravelled. The main conclusions drawn are as follows:

1. Differing from the Cu–Ag two-CS-NP sintering model, this research on the sintering of the multiple-CS-NP model exhibits an accurate description of agglomeration and pore elimination. Simultaneous interactions with multiple particles accelerate the sintering process in simulations.

2. For smaller CS NPs ($r_c < 8a_{Ag}$), solid surface diffusion dominates sintering at an intermediate temperature ($T_{room} < T < T_{sm}$), while plastic deformation plays a significant role at the T_{room}; liquid surface diffusion is deactivated after recrystallization at T_{sm}. Solid surface diffusion can induce continuous pore narrowing and elimination at T_{sm} in larger NPs ($r_c > 11a_{Ag}$).

3. Activated interfacial atoms induced by lattice mismatch and interfacial interaction contribute to a higher densification, and thus a higher bonding strength in multiple CS NPs sintered structures, compared to the pure Ag NP sintered structures.

4. E_{100}, σ_{YS}, and ν_{100} of the NP-sintered structure under T_{sm} are positively correlated with grain size, but negatively correlated

with porosity. In general, the metallic glass structure yields a lower E_{100} and σ_{YS}, but identical ν_{100}, compared with nanoporous crystallized structures. In terms of thermodynamics properties, the β_T also has a negative dependency on porosity while the α_p and c_v are independent of porosity and grain size.

This research illustrates a more realistic sintering scheme for the multiple-CS-NP model at various critical temperatures than the two-CS-NP sintering model. The size and temperature dependency of the properties of the final sintered structures are investigated to provide a theoretical basis and roadmap for selecting suitable NP size and temperature to meet specific property requirements. These findings corroborate our previous research on the sintering dynamics of the Cu–Ag two-CS-NP model. Further simulations for the effects of relative crystallographic orientation and size distribution should be performed to gain an integrative insight into Cu–Ag CS NP sintering.

Acknowledgements

This work utilized the resources of Extreme Science and Engineering Discovery Environment (XSEDE), which is supported by National Science Foundation Grant number ACI-1053575. We are thankful for the fruitful insight and discussions with Dr Anming Hu. J.W. appreciates the great efforts of Drew C. Marable and Ali Yousefzadi Nobakht in professional assistance to significantly improve the quality of this manuscript. J.W. also acknowledges helpful discussions with Dr Delong Ma, Denzel Bridges, Yongchao Yu, Shutong Wang, Chaoli Ma, Suhong Zhang, and Zhiming Liu, regarding the topic of scientific writing.

References

1 S. Ding, Y. Tian, Z. Jiang and X. He, *AIP Adv.*, 2015, **5**, 057120.
2 F. Gao, S. Mukherjee, Q. Cui and Z. Gu, *J. Phys. Chem. C*, 2009, **113**, 9546–9552.
3 K. N. Thakkar, S. S. Mhatre and R. Y. Parikh, *Nanomedicine*, 2010, **6**, 257–262.
4 P. Peng, A. Hu, A. P. Gerlich, G. Zou, L. Liu and Y. N. Zhou, *ACS Appl. Mater. Interfaces*, 2015, **7**, 12597–12618.
5 L. Lin, L. Liu, P. Peng, G. Zou, W. W. Duley and Y. N. Zhou, *Nanotechnology*, 2016, **27**, 125201.
6 B. Buesser, A. J. Grohn and S. E. Pratsinis, *J. Phys. Chem. C*, 2011, **115**, 11030–11035.
7 R. Strobel and S. E. Pratsinis, *J. Mater. Chem.*, 2007, **17**, 4743–4756.
8 S. Magdassi, M. Grouchko, O. Berezin and A. Kamyshny, *ACS Nano*, 2010, **4**, 1943–1948.
9 T. H. J. Van Osch, J. Perelaer, A. W. M. De Laat and U. S. Schubert, *Adv. Mater.*, 2008, **20**, 343–345.
10 S. Sivaramakrishnan, P. J. Chia, Y. C. Yeo, L. L. Chua and P. K. Ho, *Nat. Mater.*, 2007, **6**, 149–155.
11 D. Kim, S. Jeong, B. K. Park and J. Moon, *Appl. Phys. Lett.*, 2006, **89**, 264101.
12 W. Xie, Y. Zheng, J. Kuang, Z. Wang, S. Yi and Y. Deng, *Russ. J. Phys. Chem. A*, 2016, **90**, 848–855.
13 H. T. Hai, H. Takamura and J. Koike, *J. Alloys Compd.*, 2013, **564**, 71–77.
14 M. Tsuji, S. Hikino, Y. Sano and M. Horigome, *Chem. Lett.*, 2009, **38**, 518–519.
15 M. Miyakawa, N. Hiyoshi, M. Nishioka, H. Koda, K. Sato, A. Miyazawa and T. M. Suzuki, *Nanoscale*, 2014, **6**, 8720–8725.
16 J. Sarkar, M. Bhattacharyya, R. Kumar, N. Mandal and M. Mallik, *Adv. Sci. Lett.*, 2016, **22**, 193–196.
17 J. Xu, R. Sakanoi, Y. Higuchi, N. Ozawa, K. Sato, T. Hashida and M. Kubo, *J. Phys. Chem. C*, 2013, **117**, 9663–9672.
18 A. Hu, J. Y. Guo, H. Alarifi, G. Patane, Y. Zhou, G. Compagnini and C. X. Xu, *Appl. Phys. Lett.*, 2010, **97**, 153117.
19 E. Marzbanrad, A. Hu, B. Zhao and Y. Zhou, *J. Phys. Chem. C*, 2013, **117**, 16665–16676.
20 S. Jiang, Y. Zhang, Y. Gan, Z. Chen and H. Peng, *J. Phys. D: Appl. Phys.*, 2013, **46**, 335302.
21 P. Grammatikopoulos, C. Cassidy, V. Singh, M. Benelmekki and M. Sowwan, *J. Mater. Sci.*, 2013, **49**, 3890–3897.
22 B. J. Henz, T. Hawa and M. Zachariah, *Mol. Simul.*, 2009, **35**, 804–811.
23 K. Nakao, T. Ishimoto and M. Koyama, *J. Phys. Chem. C*, 2014, **118**, 15766–15772.
24 B. Cheng and A. H. W. Ngan, *Comput. Mater. Sci.*, 2013, **74**, 1–11.
25 P. Zeng, S. Zajac, P. C. Clapp and J. A. Rifkin, *Mater. Sci. Eng., A*, 1998, **252**, 301–306.
26 J. S. Raut, R. B. Bhagat and K. A. Fichthorn, *Nanostruct. Mater.*, 1998, **10**, 837–851.
27 J. Xu, S. Bai, Y. Higuchi, N. Ozawa, K. Sato, T. Hashida and M. Kubo, *J. Mater. Chem. A*, 2015, **3**, 21518–21527.
28 J. Wang and S. Shin, *J. Nanopart. Res.*, 2017, **19**, 53.
29 J. Wang, S. Shin and A. Hu, *J. Phys. Chem. C*, 2016, **120**, 17791–17800.
30 R. M. German, *Sintering Theory and Practice*, Wiley-Interscience, New York, 1996.
31 S. Plimpton, *J. Comput. Phys.*, 1995, **117**, 1–19.
32 J. Towns, T. Cockerill, M. Dahan, I. Foster, K. Gaither, A. Grimshaw, V. Hazlewood, S. Lathrop, D. Lifka, G. D. Peterson, R. Roskies, J. R. Scott and N. Wilkins-Diehr, *Comput. Sci. Eng.*, 2014, **16**, 62–74.
33 M. S. Daw and M. I. Baskes, *Phys. Rev. B: Condens. Matter Mater. Phys.*, 1984, **29**, 6443–6453.
34 P. L. Williams, Y. Mishin and J. C. Hamilton, *Modell. Simul. Mater. Sci. Eng.*, 2006, **14**, 817–833.
35 L. Verlet, *Phys. Rev.*, 1967, **159**, 98–103.
36 S. Li, W. Qi, H. Peng and J. Wu, *Comput. Mater. Sci.*, 2015, **99**, 125–132.
37 P. Song and D. Wen, *J. Phys. Chem. C*, 2010, **114**, 8688–8696.
38 R. Huang, Y. Wen, Z. Zhu and S. Sun, *J. Phys. Chem. C*, 2012, **116**, 11837–11841.
39 Z. Yang, X. Yang, Z. Xu and S. Liu, *Phys. Chem. Chem. Phys.*, 2009, **11**, 6249–6255.
40 J. Tang and J. Yang, *J. Nanopart. Res.*, 2015, **17**, 299.
41 Z. Yang, X. Yang and Z. Xu, *J. Phys. Chem. C*, 2008, **112**, 4937–4947.

42 S. Alavi and D. L. Thompson, *J. Phys. Chem. A*, 2006, **110**, 1518–1523.
43 Y. Tamura and N. Arai, *Mol. Simul.*, 2015, **41**, 905–912.
44 P. Song and D. Wen, *J. Nanopart. Res.*, 2009, **12**, 823–829.
45 K. B. Wiberg, *J. Am. Chem. Soc.*, 1965, **87**, 1070–1078.
46 D. Keffer and P. Adhangale, *Chem. Eng. J.*, 2004, **100**, 51–69.
47 R. Xiong, K. Odbadrakh, A. Michalkova, J. P. Luna, T. Petrova, D. J. Keffer, D. M. Nicholson, M. A. Fuentes-Cabrera, J. P. Lewis and J. Leszczynski, *Sens. Actuators, B*, 2010, **148**, 459–468.
48 A. Mashreghi, *Comput. Mater. Sci.*, 2012, **62**, 60–64.
49 M. H. Ghatee and K. Shekoohi, *Fluid Phase Equilib.*, 2013, **355**, 114–122.
50 V. M. Dadarlat and C. B. Post, *J. Phys. Chem. B*, 2001, **105**, 715–724.
51 M. Kaviany, *Heat Transfer Physics*, Cambridge University Press, New York, 2014.
52 R. Z. Li, A. Hu, D. Bridges, T. Zhang, K. D. Oakes, R. Peng, U. Tumuluri, Z. Wu and Z. Feng, *Nanoscale*, 2015, **7**, 7368–7377.
53 G. Guenther and O. Guillon, *J. Mater. Sci.*, 2014, **49**, 7915–7932.
54 Y. Shibuta and T. Suzuki, *Chem. Phys. Lett.*, 2007, **445**, 265–270.
55 J. G. Hou, B. Wang, J. Yang, K. Wang, W. Lu, Z. Li, H. Wang, D. M. Chen and Q. Zhu, *Phys. Rev. Lett.*, 2003, **90**, 246803.
56 A. Dutta, *Rev. Adv. Mater. Sci.*, 2014, **39**, 25–33.
57 H. Zhu, *Philos. Mag. Lett.*, 1996, **73**, 27–33.
58 S. Arcidiacono, N. R. Bieri, D. Poulikakos and C. P. Grigoropoulos, *Int. J. Multiphase Flow*, 2004, **30**, 979–994.
59 G. J. Ackland and A. P. Jones, *Phys. Rev. B: Condens. Matter Mater. Phys.*, 2006, **73**, 054104.
60 W. Lechner and C. Dellago, *J. Chem. Phys.*, 2008, **129**, 114707.
61 A. Stukowski, *Modell. Simul. Mater. Sci. Eng.*, 2012, **20**, 045021.
62 M. Tavakol, M. Mahnama and R. Naghdabadi, *Mater. Manuf. Processes*, 2015, **30**, 1397–1402.
63 Z. Z. Fang and H. Wang, *Int. Mater. Rev.*, 2013, **53**, 326–352.
64 S. Shin, M. Kaviany, T. Desai and R. Bonner, *Phys. Rev. B: Condens. Matter Mater. Phys.*, 2010, **82**, 081302.
65 G. Antczak and G. Ehrlich, *Surface Diffusion: Metals, Metal Atoms, and Clusters*, Cambridge University Press, New York, 2010.
66 E. A. Oliber, C. Cugno, M. Moreno, M. Esquivel, N. Haberkorn, J. E. Fiscina and C. J. R. G. Olivera, *Matéria*, 2003, **8**, 350–357.
67 R. E. Hoffman and D. Turnbull, *J. Appl. Phys.*, 1951, **22**, 634–639.
68 M. A. Asoro, P. J. Ferreira and D. Kovar, *Acta Mater.*, 2014, **81**, 173–183.
69 H. S. Kim and M. B. Bush, *Nanostruct. Mater.*, 1999, **11**, 361–367.
70 N. Wang, Z. Wang, K. T. Aust and U. Erb, *Acta Metall. Mater.*, 1995, **43**, 519–528.
71 T.-Y. Kim, J. E. Dolbow and E. Fried, *Int. J. Solids Struct.*, 2012, **49**, 3942–3952.
72 Q. Li, *Mater. Lett.*, 2007, **61**, 3323–3328.
73 D. V. Louzguine-Luzgin, T. Saito, J. Saida and A. Inoue, *J. Mater. Res.*, 2011, **23**, 515–522.
74 X. Cheng, J. Zhang, H. Zhang and F. Zhao, *J. Appl. Phys.*, 2013, **114**, 084310.
75 J. Wang, P. D. Hodgson, J. Zhang, W. Yan and C. Yang, *J. Mater. Process. Technol.*, 2009, **209**, 4601–4606.